Title: Scaling up aqueous processing of A-site deficient strontium titanate for SOFC anode supports

Authors: Maarten C. Verbraeken, Bhaskar Reddy Sudireddy, Viacheslav Vasechko, Mark Cassidy, Tânia Ramos, Jürgen Malzbender, Peter Holtappels, John T.S. Irvine

PII: S0955-2219(17)30807-5
DOI: https://doi.org/10.1016/j.jeurceramsoc.2017.11.057
Reference: JECS 11603

To appear in: *Journal of the European Ceramic Society*

Received date: 28-8-2017
Revised date: 26-11-2017
Accepted date: 28-11-2017

Please cite this article as: Verbraeken Maarten C, Sudireddy Bhaskar Reddy, Vasechko Viacheslav, Cassidy Mark, Ramos Tânia, Malzbender Jürgen, Holtappels Peter, Irvine John T.S.Scaling up aqueous processing of A-site deficient strontium titanate for SOFC anode supports.*Journal of The European Ceramic Society* https://doi.org/10.1016/j.jeurceramsoc.2017.11.057

Scaling up aqueous processing of A-site deficient strontium titanate for SOFC anode supports

Maarten C. Verbraeken[a], Bhaskar Reddy Sudireddy[b], Viacheslav Vasechko[c], Mark Cassidy[a], Tânia Ramos[b], Jürgen Malzbender[c], Peter Holtappels[b], John T.S. Irvine[a]

[a] *School of Chemistry, University of St Andrews, North Haugh, St Andrews, KY16 9ST, United Kingdom*

[b] *DTU Energy Conversion and Storage, Technical University of Denmark, Frederiksborgvej 399, DK-4000 Roskilde, Denmark*

[c] *Forschungszentrum Jülich GmbH, Institute of Energy and Climate Research (IEK-2), DE-52425 Jülich, Germany*

Abstract

All ceramic anode supported half cells of technically relevant scale were fabricated in this study, using a novel strontium titanate anode material. The use of this material would be highly advantageous in solid oxide fuel cells due to its redox tolerance and resistance to coking and sulphur poisoning. Successful fabrication was possible through aqueous tape casting of both anode support and electrolyte layers and subsequent lamination. Screen printing of electrolyte layers onto green anode tapes was also attempted but resulted in cracked electrolyte layers upon firing. Microstructural, electrical and mechanical properties of anode supports and half cells will be discussed. The use of two different commercial titanate powders with nominal identical, but in reality different stoichiometries, strongly affect electrical and mechanical properties. Careful consideration of such variations between powder suppliers, and batches of the same supplier, is critical for the successful implementation of ceramic anode supported solid oxide fuel cells.

Keywords: Solid oxide fuel cells
Alternative anodes
Perovskites
Tape casting
Co-firing

Introduction

Conventional state-of-the-art Ni cermet anodes for solid oxide fuel cells (SOFCs) perform well in hydrogen and high steam reformate fuels [1], but still suffer from a number of drawbacks. Their poor redox stability, tendency for coking in hydrocarbon fuels and low sulphur tolerance has led many researchers to look for alternative anode materials. One promising approach is to replace the cermet with an electronically conducting ceramic to provide both structural support and current collection, whereas electrocatalytic activity can be obtained through impregnation of precursors solutions of electrocatalytically active materials into the porous scaffold. A-site deficient strontium titanates show high n-type conductivity and therefore offer promise as the electronically conducting backbone. Previous work has

shown promising results for a La and Ca co-doped $SrTiO_3$ anode in an electrolyte supported cell (ESC) configuration, into which nickel and ceria were impregnated to serve as fuel oxidation catalysts. Fuel cell performances in hydrogen were similar to those for Ni-cermet anodes, but with much improved redox stability [2–4].

The A-site deficient $La_{0.20}Sr_{0.25}Ca_{0.45}TiO_3$ ($LSCT_{A-}$) shows reasonable mechanical strength [5] and may therefore also be suitable as anode support material in an anode supported cell (ASC) design, allowing for SOFC operation at lower temperatures. To this end, an aqueous tape casting process was developed, as an environmentally friendly alternative to the organics based process [6,7]. Also, the aqueous processing allows for using a wider range of polymeric pore formers that would otherwise dissolve in the solvent. This in turn allows for a more precise control of the microstructure of the porous scaffold for optimal electrode performance. Although strontium titanates have been used previously in tape cast electrodes, the resulting cells are commonly small (< 1 cm^2) and the anode supports are typically composites of stabilised zirconia, which provides structural support and ionic conductivity [8,9] .

In this study we report on the very first scale-up attempt of single phase $LSCT_{A-}$ anode supported SOFCs, from the laboratory scale casting process at the University of St Andrews to the pre-pilot scale environment at the Technical University of Denmark, DTU (Roskilde) [10]. Apart from enabling fabrication of larger cells, the optimised environment at DTU should allow for better control of the process, ultimately leading to superior ceramics. Half cells are prepared by depositing thin electrolyte layers onto tape cast anode supports through either screen printing or lamination. Resulting ceramics were analysed for their microstructure and mechanical properties. The electrical properties of the ceramics, prepared by both small and large scale processing, were finally assessed and compared with previous reports.

The ultimate aim of the work was to produce all-ceramic half cells at an industrially relevant scale using industrially relevant processing techniques, as part of a proof-of-concept project. The time constraints imposed by such projects forced the employment of a very pragmatic approach, rather than a fully systematic bottom-up strategy. The results reported in this manuscript will reflect this and should therefore be regarded as a report on the practical development of full scale strontium titanate supported SOFC, the novelty of which is of interest in itself. To our knowledge, the largest reported cells of this kind are 5 x 5 cm^2, produced by the less scalable process of warm pressing, rather than tape casting [11,12].

Experimental

Powders

Two $LSCT_{A-}$ ($La_{0.20}Sr_{0.25}Ca_{0.45}TiO_3$) powders were used in this study. Powder A was synthesised by Topsoe Fuel Cells A/S (TOFC), Denmark, using the drip pyrolysis method [13]. The second, powder B, was purchased from CerPoTech AS, Norway, who use a comparable solution based method, namely spray pyrolysis. The resulting powders were nanosized, high surface area powders (~40 m^2/g, measured by BET, Tristar II 3020, Micromeritics, UK). The powders were calcined in air for 5 hours at 1200 – 1300°C prior to ceramic processing, resulting in BET surface areas of 2 – 0.2 m^2/g as described in Table 1. The resulting particle size distributions, as obtained after the 24 hour de-agglomeration step during ceramic slurry preparation (see Aqueous tape casting), were analysed using a Malvern Mastersizer 2000, connected to a Hydro 2000S sampler and are presented in Table 1. Yttria stabilized zirconia powder (8-YSZ, $Zr_{0.85}Y_{0.15}O_{1.92}$) for the electrolyte layers was purchased from Pi-Kem Ltd, and had a d_{50} particle size of 0.2 μm, with a BET surface area of ~7 m^2/g.

Phase characterisation was carried out by X-ray diffraction (Empyrean, Panalytical (NL), Cu $K\alpha_1$ radiation) as well as X-ray Fluorescence (XRF, Spectro XEPOS, Germany) and Energy Dispersive X-ray Spectroscopy (Oxford Scientific, USA).

Table 1: Particle size distributions and BET surface areas for powder A and B, calcined at different temperatures

$LSCT_{A-}$ powder	Calcination temp. (°C)	Particle size (μm)			BET surface area (m^2/g)
		d_{10}	d_{50}	d_{90}	
A	Uncalcined	-	-	-	36
A	1200	0.71	2.1	5.2	1.6
A	1250	0.91	3.2	7.9	0.5
A	1300	1.1	4.2	11	0.2
B	Uncalcined	-	-	-	44
B	1200	0.97	2.0	3.9	1.6
B	1250	-	-	-	1.0
B	1300	1.5	3.1	5.8	0.7

Processing

Anode supports were produced by aqueous tape casting, whereas both screen printing and aqueous tape casting were used to deposit thin dense electrolyte layers on top of the green anode supports. Screen printed or laminated half cells were subsequently co-fired in air at 1300 – 1325°C for 2 hours.

Aqueous tape casting

Hypermer KD6 (Uniqema) was used as the dispersant, with deionised water as the solvent. Polyethylene glycol (PEG, av. M_w 300, Sigma Aldrich) and glycerol (Alfa Aesar) were used as plasticisers, with a high molecular weight PVA (polyvinyl alcohol, 87 – 89 % hydrolysed, M_w = 88,000 – 97,000 g/mol, Alfa Aesar) as the binder. A molecular defoamer (DF002, Polymer Innovations) was finally added to prevent extensive foaming and to act as a releasing agent from the Mylar carrier. The tape casting slips were produced in a three-step process. First, the ceramic powder was dispersed and de-agglomerated in deionised water by rotary ball milling for 24 hours. After this step the plasticisers and binder were mixed in by ball milling. This was done at a reduced speed to prevent degradation of the binder polymer. The PVA was pre-dissolved in deionised water to reach a 15 wt.% solution. Finally, the slip was de-aired by either slow rolling or by applying a mild vacuum. Tapes were cast onto an uncoated Mylar carrier film and subsequently air dried. The small scale process at St Andrews uses a benchtop tape caster, model TTC1200, Richard E. Mistler Inc., with single doctor blade, whereas a full scale caster with double blade was used at DTU.

Screen printing

The YSZ screen printing ink consisting of propylene glycol and PVP K90 binder, as previously discussed in [7], was produced by planetary ball milling. Printing was carried out on a DEK 248 screen printer.

Characterisation of slurries and ceramics

Rheological behaviour of tape slips, ink vehicles and inks was measured on a Brookfield DVIII Ultra Rheometer using a small sample adapter (SC4-13R chamber with SC4-21 spindle). All viscosity data was recorded at room temperature. The microstructures of co-sintered ceramics were studied by SEM (FEG-SEM, Jeol JSM 6700F and Supra, Carl Zeiss,

Germany) and Hg porosimetry (Quantachrome Poremaster 60GT, USA). Image analysis through the Fiji software package was additionally used for microstructural characterisation.
The electrical properties of the sintered anode supports were tested by four terminal Van der Pauw DC method [14]. Samples were reduced in situ in 5% H_2 / 95% argon at 850°C. Impregnation techniques were further used to enhance the electrical properties of the porous anode supports. To this end, 10 wt.% of various forms of ceria (CeO_2, $Ce_{0.8}Gd_{0.2}O_{1.9}$ and $Ce_{0.5}Zr_{0.5}O_2$) were introduced into the porous scaffolds using the respective nitrate solutions in ethanol ($Ce(III)(NO_3)_3$, $Gd(III)(NO_3)_3$, Sigma Aldrich and Ce(III) 2-ethylhexanoate, Zr(IV) 2-ethylhexanoate, Alfa Aesar), with appropriate additions of acetyl acetone (Alfa Aesar) to stabilise the solutions. Added weight percentages were verified using gravimetric methods.
Mechanical testing was performed at room temperature on both sintered anode supports and co-sintered half cells by ring-on-ring bending experiments, as previously discussed in [5].

Results and discussion

Powder (Phase analysis)
Both $LSCT_{A-}$ powders were characterised by X-ray diffraction after air calcination at 1300°C; the results are shown in Figure 1. Powder A could be indexed using the orthorhombic spacegroup *P b n m*, with lattice parameters a = 5.464 Å, b = 5.465 Å, c = 7.734 Å, which is in good agreement with previously reported data by Aljaberi and Irvine [15], despite slightly larger lattice parameters. There are some minor additional reflections, suggesting the presence of a secondary phase. In powder B, however, even after calcination at 1300°C these additional reflections (at 27.4°, 36.0° and 54.3°, marked in Figure 1) are significantly more dominant. The predominant impurity in both powders seems to be rutile TiO_2 and from Rietveld refinement its content can be estimated to be less than 0.1 mol.% for powder A, whereas for powder B it is between 5 – 6 mol.%. The main phase of powder B is still best refined using the orthorhombic spacegroup *P b n m*, with a = 5.473 Å, b = 5.463 Å and c = 7.748 Å. The extra rutile phase can also clearly be seen by SEM in backscattered mode (Figure 2). Both XRF and EDX elemental analyses suggest that powder B exhibits too large an A-site deficiency (15 – 20 % as compared to 10 – 13% in powder A and in-house synthesised powders by solid state route (SSR), see Table 2), promoting the segregation of TiO_2 rich phases. Assuming the presence of 5 – 6 mol.% of rutile, the actual level of A-site deficiency in the primary strontium titanate phase of powder B is estimated to be 13 – 14%, which would also explain the larger unit cell volume. This can affect the defect chemistry of the material and thus its physical properties, such as electrical behaviour and mechanical properties [16].

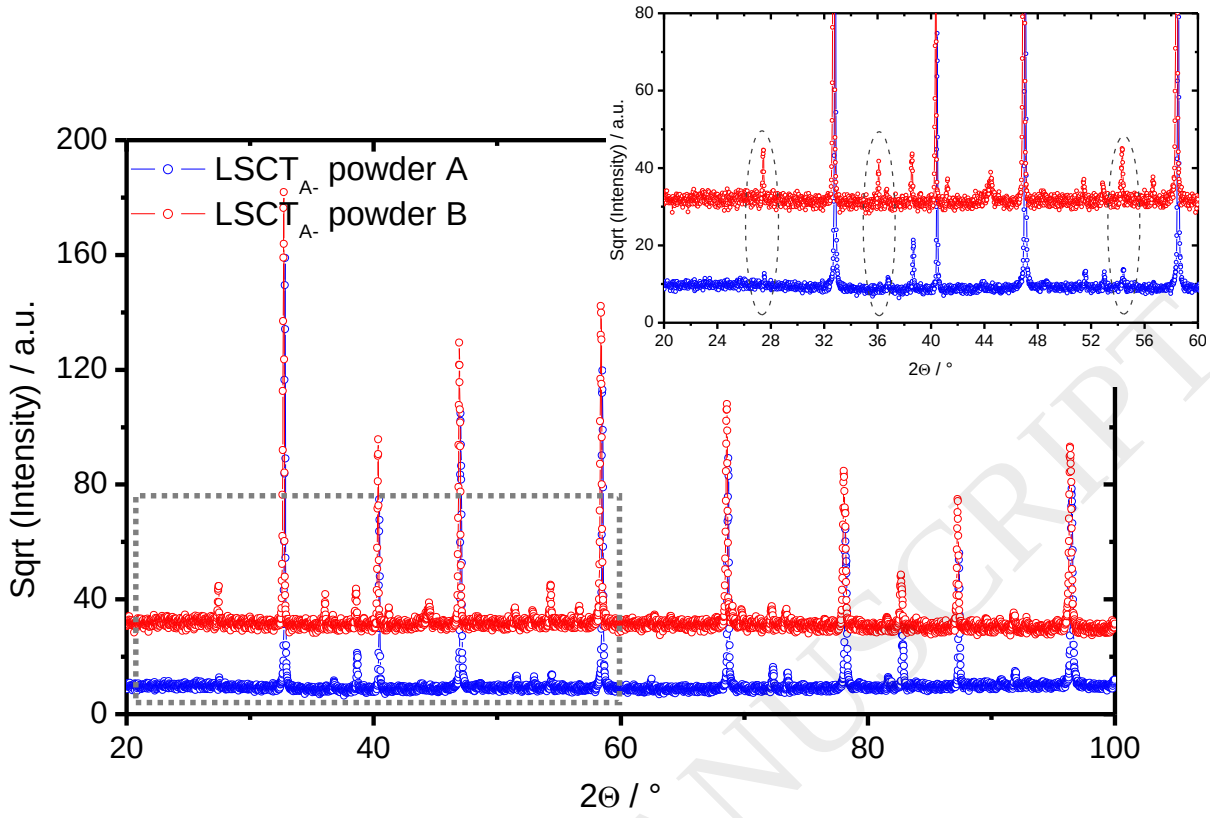

Figure 1: XRD patterns for LSCT$_{A-}$ from powder A and B calcined at 1300°C, showing major extra reflections from rutile in the latter at 27.4°, 36.0° and 54.3° (circled in zoomed section).

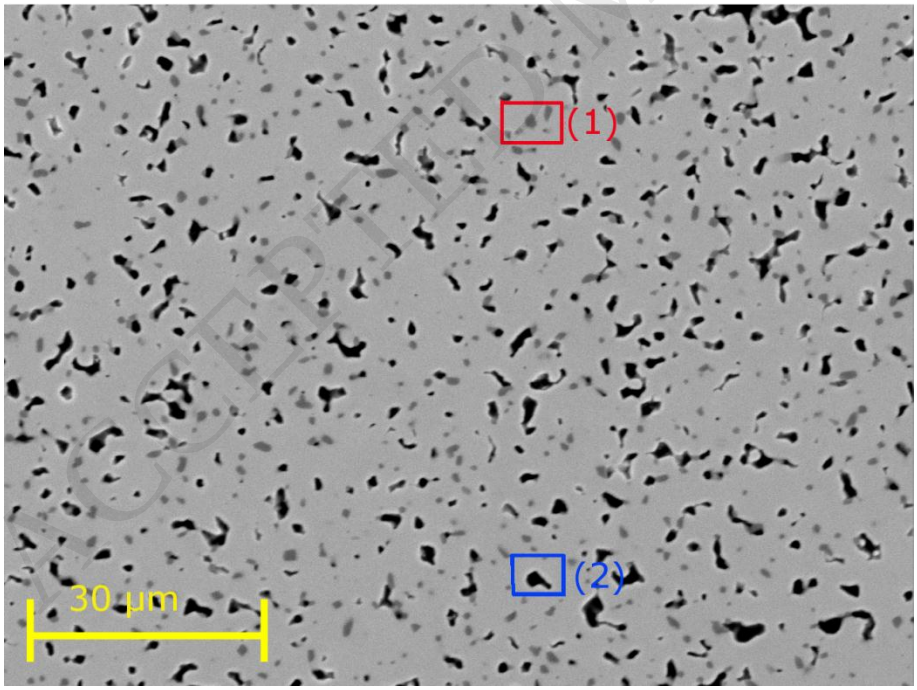

Figure 2: SEM backscattered micrograph of LSCT$_{A-}$ ceramic from powder B. Black regions are pores (blue box labelled 2), darker grey areas are secondary phase (rutile, red box labelled 1).

Table 2: Elemental analysis by XRF and EDX on powders A and B, as well as on in-house synthesised $LSCT_{A-}$

	La (at%)	Sr (at%)	Ca (at%)	Ti (at%)	A/B
Powder A (XRF)	4.0	5.1	8.8	20.6	0.87
Powder A (EDX)	4.3	4.6	8.5	19.5	0.90
Powder B (XRF)	3.9	5.0	8.4	21.6	0.80
Powder B (EDX)	4.4	4.8	9.4	22.1	0.85
In-house SSR (XRF)	4.1	5.0	8.6	19.9	0.89
Theoretical	4.1	5.1	9.2	20.4	0.90

Particle size distribution

The particle size distribution of the two different $LSCT_{A-}$ powders could be controlled through calcination temperature. Since both have been synthesised through comparable solution based routes, which yield similar nanosized powders, their respective particle size distributions as a function of temperature are also very similar. As Figure 3a and b show, despite comparable d_{50} values at identical calcination conditions, powder B yields a narrower particle size distribution than powder A. As a previous study has shown, $LSCT_{A-}$ is a highly sinteractive material, owing to its A-site deficiency and calcium content [6]. The effect of A-site deficiency on sinterability is evident from Figure 3b, showing a smaller fine fraction for powder B, owing to its higher A-site deficiency as compared to powder A. Due to the sinteractivity of $LSCT_{A-}$, a coarser powder with a d_{50} between 1 – 4 µm (target d_{10} ~0.5 and d_{90} ~10 µm) is desirable in terms of thick film processing, as the resulting anode support requires ample porosity to prevent gas transport limitations during SOFC operation, also enabling impregnation of the anode. At the same time, firing temperatures will be constrained due to the co-sintering with the electrolyte layer, imposing a lower limit to ensure densification of the latter to prevent the loss of Nernst potential.

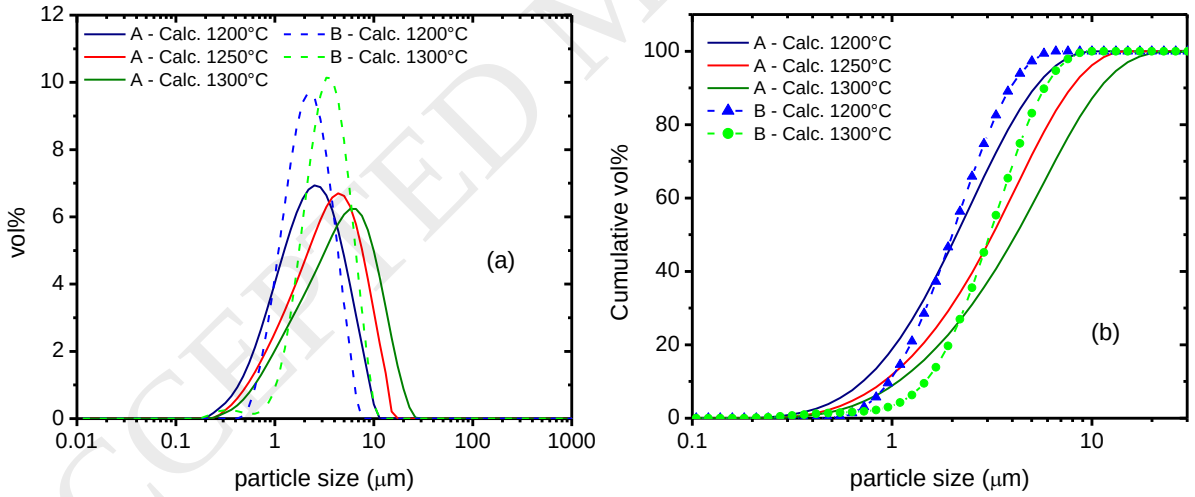

Figure 3: Particle size (a) and cumulative (b) distribution for $LSCT_{A-}$ calcined in air at various temperatures.

Rheology

All aqueous tapes in this study comprise a polyvinyl alcohol (PVA) based binder system. The PVA is pre-dissolved in de-ionised water before its addition to the slips. Figure 4 shows the dependence of viscosity on the PVA concentration, which is in agreement with literature reports [17].

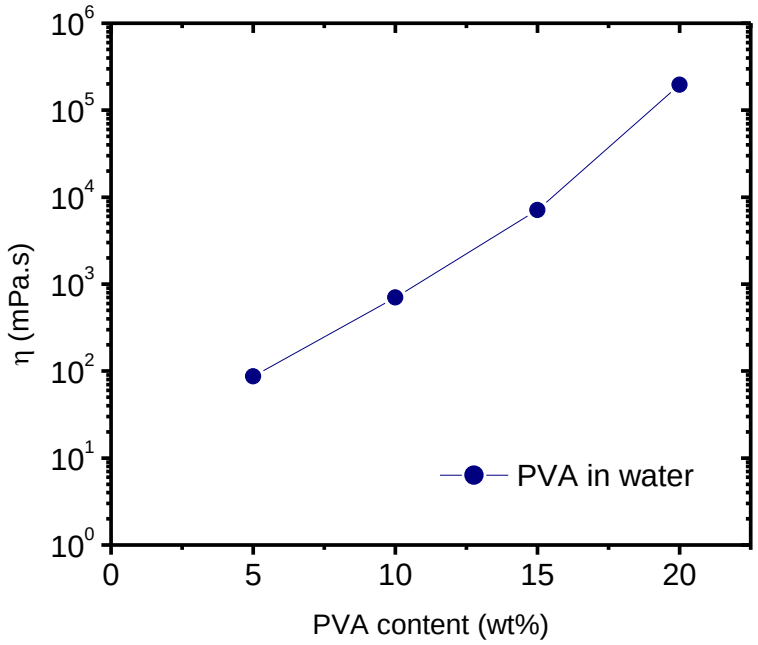

Figure 4: Viscosity of binder solution as a function of PVA content in water.

Table 3: Typical tape casting slip compositions for the different ceramics.

	$LSCT_{A-}$ (vol.% of ceramic)	**8-YSZ (vol.% of ceramic)**
Deionised water	190	300
Hypermer KD-6	9.4	18
Polyethylene glycol	32	32
Glycerol	56	57
PVA	39	50
Polymer Innovations DF002	4.7	7.2

A typical recipe for $LSCT_{A-}$ and YSZ aqueous tapes is given in Table 3. Although many parameters can be varied and optimised to great detail in this type of slurry development, we have focused on making changes to the solids component, by varying calcination temperatures and solids content. The polymer matrix as described in Table 3 was optimised throughout the project to yield suitable rheological behaviour of the slips as well as strong and flexible tapes, which are easy to handle and manipulate. The effect of solids loading and particle size on the aqueous slips' rheological behaviour has been studied in more detail. The rheological behaviour of the aqueous tape casting slips is presented as shear stress versus shear rate curves, as shown in Figure 5 and Figure 6. All the slips showed shear thinning behaviour, which is appropriate for the tape casting process [18]. The effect of calcination temperature, thus particle size, on the rheology of slips is shown in Figure 5. An initial solids loading of 66 wt.% was used for all slips in this experiment, using $LSCT_{A-}$ from powder A. Lower calcination temperatures than 1200°C were not used in this study, due to the resulting increased sinteractivity, which is deemed unsuitable for achieving porous anode supports. As expected, the viscosities of slips increased with decreasing particle size, due to the increase in surface area and therefore inter-particle interaction. However, the effect was small and not suitable for an efficient adjustment of the slip rheology. High viscosity $LSCT_{A-}$ slips are desirable in order to enable casting thick (0.5 – 1 mm dried thickness) films and avoid the

need for laminating various tapes. Figure 6 shows the dependence of viscosity on initial ceramics loading (during de-agglomeration stage). The data in this graph was obtained on powder B, calcined at 1300°C. Both viscosity data and particle size analysis suggest that this particular powder can be dispersed up to an initial 80 wt.% solids loading. The viscosity reaches around 2.6 Pa·s at a shear rate of 5 s^{-1}. This is still at the lower end of enabling thick film casting and was probably caused by the addition of water during the second stage, through the pre-dissolved binder. Further optimisation of the slip composition would therefore be required.

Figure 6 also shows the dependence of viscosity on solids loading for the sub-micron 8-YSZ powder as used in this study. Higher viscosities were more easily obtained, due to the high surface area as compared to the strontium titanate powder (7 m^2/g vs. 0.2 – 2 m^2/g, respectively). Lower viscosities are preferable for casting thinner films however, as this could prevent the entrapment of air bubbles, which could lead to pinholes in the final electrolyte layer.

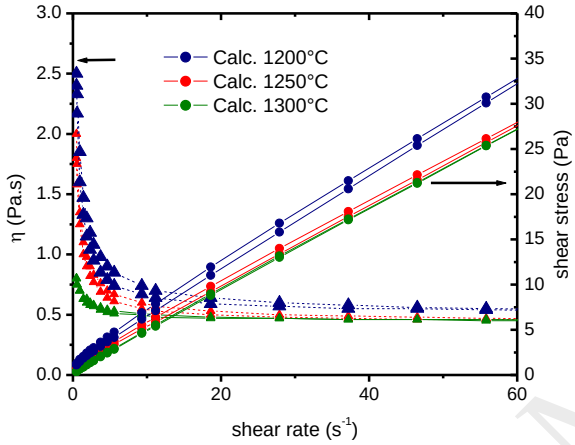

Figure 5: Effect of calcination temperature on slip viscosity. $LSCT_{A-}$ powder A used in this graph

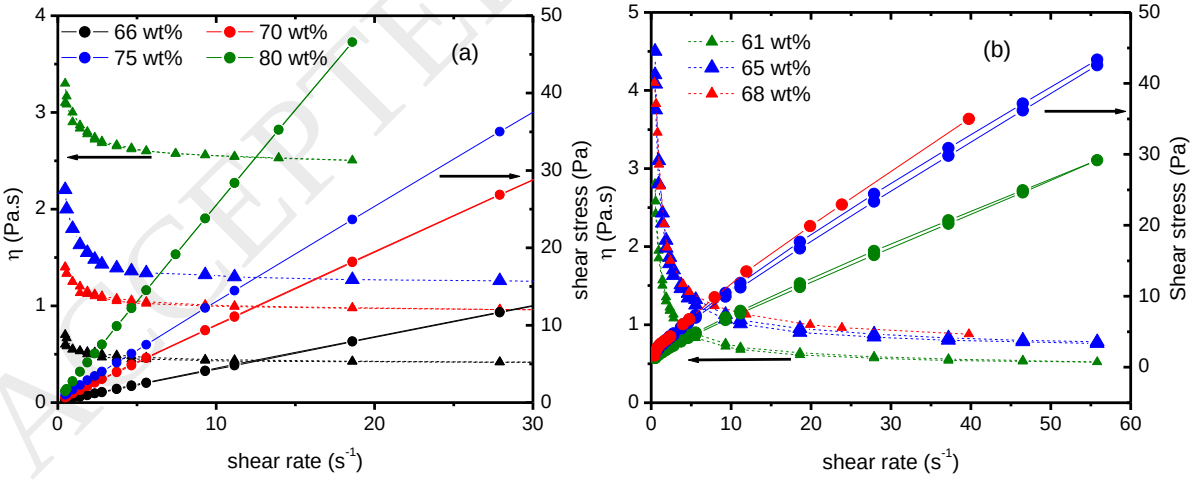

Figure 6: Effect of solids loading on slip viscosity. Left (a): $LSCT_{A-}$ for anode support tapes (powder B used in this graph). Right (b): 8-YSZ for electrolyte tapes.

Microstructural characterisation - small scale processing

The facilities at St Andrews allow for the production of laminated green tapes up to 10 x 10 cm^2. Due to the limited size of the available furnaces, ceramics of up to 5 x 5 cm^2 could be

produced upon firing. Image analysis was performed on various sintered ceramic tapes cast from both powders with differing calcination temperatures, as well as from slips with varying solids content. All ceramics were fired at 1300°C – 1325°C for 2 hours. Table 4 shows the microstructural characteristics of these ceramics. Despite limited data points, it seems that calcining at lower temperatures results in denser microstructures with smaller pores. When comparing the microstructures for $LSCT_{A-}$ (powder A) calcined at 1250°C and 1300°C, the porosity increased from 17% to 25%, respectively, with the mean pore size increasing from 1.3 to 1.8 µm. $LSCT_{A-}$ calcined at lower temperatures is expected to be more sinter active, which results in more shrinkage on sintering. Additionally, calcination at 1300°C was observed to give rise to a small degree of sintering during the calcination process, which may have led to the formation of a small number of hard agglomerates. These agglomerates were observed during slip preparation as large lumps; despite a filtering step, it is likely that smaller agglomerates would have remained in the slips. The presence of such agglomerates in turn may have resulted in poorer dispersion and ultimately poorer powder packing during tape drying as compared to powders calcined at lower temperatures. These mechanisms would agree with the more porous microstructure observed for higher calcination temperatures. A similar, but less pronounced, observation was made for the microstructures of tapes with varying solids content. Higher solids content tapes give rise to more porous and coarser microstructures as shown in both Table 4 and Figure 7. At 80 wt.% and 66 wt.% solids loading, 22% and 20% porosity are observed, respectively. Whereas most of the pores at 66 wt.% seem to be 0.7 – 1 µm in size, at 80 wt.% the pore size distribution has shifted significantly to larger pore sizes, with the majority of pores being in the range of 2 – 9 µm. Generally a reverse trend would be expected (i.e. higher ceramic densities at higher solids loadings), which may suggest that dispersion and its stability in this aqueous system becomes difficult at higher solids loadings, leading to said poor powder packing and higher porosity.

Table 4: Microstructural characteristics of various tape cast ceramics as obtained by image analysis.

$LSCT_{A-}$ powder	Calcination temp. (°C)	Solids loading (wt.%)	Sintering temp. (°C)	Linear shrinkage (%)	Total porosity (%)	Mean pore size (µm)	Area average pore size (µm)	Pore size range (µm)
A	1250	66	1300	17	17	1.3	1.2	0.5 – 6
A	1300	66	1300	14	25	1.8	5.8	0.5 – 8
A	1250	66	1325	21	10	1.5	3.6	0.5 – 5
A	1300	66	1325	19	18	2.1	4.4	0.9 – 6
B	1300	66	1325	19	20	1.7	4.8	0.5 – 7
B	1300	75	1325	18	21	2.4	6.5	1 – 8
B	1300	80	1325	18	22	2.7	6.7	2 – 9

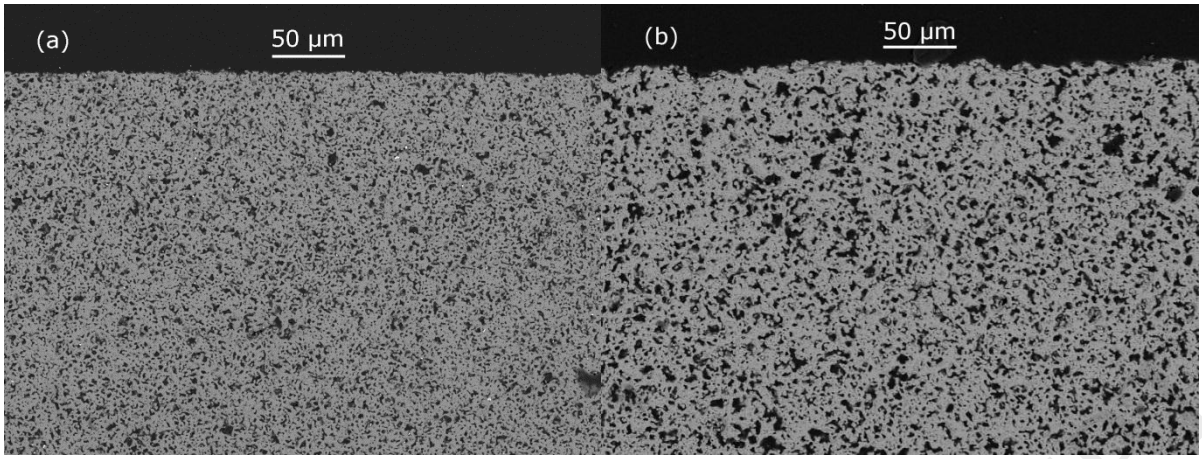

Figure 7: Microstructure of aqueous tapes using different solids loadings of $LSCT_{A-}$ (powder B, calcined at 1300°C). Left (a) 66 wt.% and right (b) 80 wt.%. Final sintering at 1325°C for 2 hours.

Microstructural characterisation - scaled up processing of half cells

Tape cast anode supports

The small scale aqueous tape casting process initially developed at University of St Andrews was successfully transferred to the large scale facilities at DTU. Due to cessation of powder production at one of our suppliers, we were unfortunately only able to use powder B for these scale-up efforts. This fact will obviously limit our ability to properly compare the two powders in terms of processing purposes and this has been taken into account when discussing the results. The scaled up process allowed production of laminated green tapes with dimensions of up to 20 x 20 cm^2. Dried green thicknesses of the tapes vary between 200 – 250 µm, with some small variation (10 – 20 µm) across the width of the tapes. Casting thicker tapes would certainly be desirable in order to avoid a necessary additional lamination step, but was not feasible during the current study, due to the relatively low viscosities of the slips (a maximum viscosity of only 0.83 Pa·s was obtained at 5 s^{-1}). The thickness variation across the width of the tape also requires further optimisation and will be the focus of future work. Figure 8a shows a cross-section of a half cell fabricated through the scaled up process at DTU. It shows a regular anode support microstructure with good connectivity of the $LSCT_{A-}$ grains. Image analysis indicates that the porosity of anode supports is around 22%, after a linear shrinkage of 20% on sintering. This value compares well with the small scale processing discussed in the previous section. The porosity may seem low as compared to conventional Ni cermet supports [19], but is in fact comparable to porosities in most as-sintered NiO/YSZ anode supports. After all, Ni cermets obtain most of their porosity during reduction of NiO under SOFC operating conditions, rather than during processing. In the case of all ceramic anode supports, no additional porosity will be obtained on reduction, so all porosity must develop during processing. When co-sintering anode support and electrolyte, careful matching of shrinkages and shrinkage rates in the two layers is necessary to ensure densification of the electrolyte whilst maintaining some degree of porosity in the anode support. This leads to an inherent compromise of around 20% porosity for the anode support as a natural result of sintering processes. However it is also acknowledged that this is lower than often observed in cermet anodes and that additional porosity maybe required in order to avoid difficulties in infiltrating catalysts and also minimising mass transport losses during operation. It is hoped to apply related work on addition of polymeric pore formers, currently underway at University of St Andrews, to the $LSCT_{A-}$ system [20]. This will allow porosity to be both increased and tailored to optimise electrochemical performance.

Screen printed electrolyte layers

The electrolyte in the half cell shown in Figure 8a was deposited by screen printing. An even and dense YSZ layer of 10 – 12 µm thickness can be seen, which adheres well to the anode support. The profilometer image taken before sintering also shows a reasonably smooth print with a surface roughness of 1 – 2 µm (Figure 8b). The screen printed layers tend to shrink too much on firing however, leading to severe cracking as evidenced by Figure 8c. Some minor reaction between anode support and electrolyte is evident as well, as indicated by the darker regions within the electrolyte layer. Alternatively this may be caused by some solvent mixing during processing (tape plasticisers and ink vehicle).

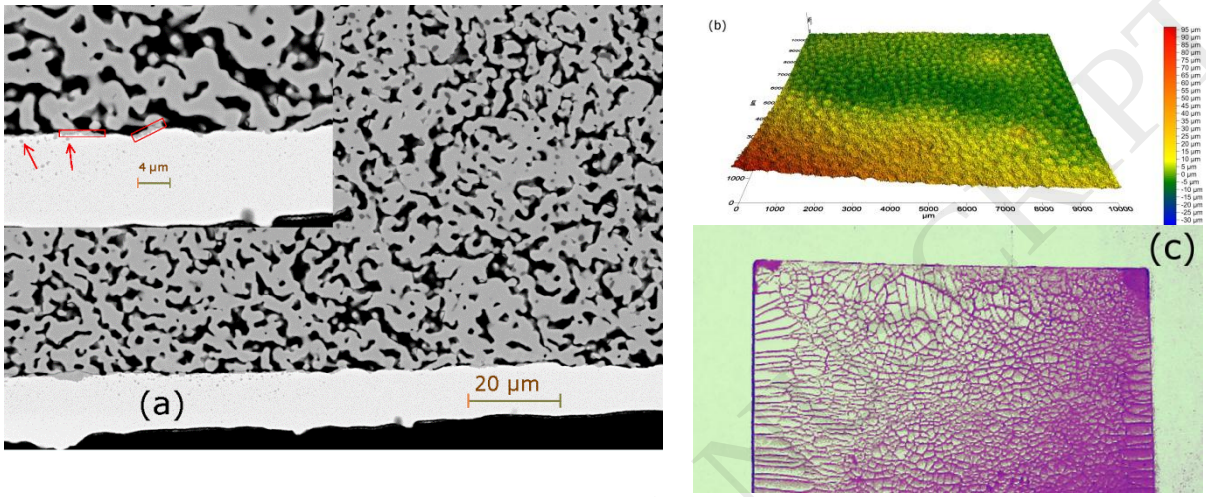

Figure 8: Scaled-up co-sintered 5 x 5 cm^2 half cell of LSCT$_{A-}$ powder B with YSZ electrolyte. Electrolyte deposited by screen printing. Assembly co-sintered at 1325°C for 2 h. Arrows in (a) highlight minor presence of dark regions indicating reaction phases after firing. Figure (b) shows profilometer data of green printed YSZ layer revealing minor surface roughness (1 – 2 µm). Figure (c) is a top-down image of the electrolyte layer after firing, showing severe cracking.

Tape cast electrolyte layers

To further improve the electrolyte quality and to solve the cracking issue, the electrolyte layers were also deposited by laminating aqueous LSCT$_{A-}$ support and thin YSZ electrolyte tapes and co-firing these assemblies. In this way, electrolyte layers with a thickness of approximately 10 µm can be deposited, which compares well to screen printed layer thicknesses. On firing, an increased linear shrinkage of 24% is observed. The resulting microstructure of these ceramics can be seen in Figure 9a, revealing a dense electrolyte with a well adhered, moderately porous anode support. No cracking of the electrolyte layers was observed as shown in Figure 9b. A much increased presence of dark regions within the electrolyte layer at the interface with LSCT support can be seen in Figure 9a as compared to Figure 8a. This suggests enhanced reaction between the two layers when laminating, as opposed to screen printing the electrolyte layer. It can also be seen that the porosity of this anode support (17% as measured by Hg porosimetry) is significantly lower than obtained by co-firing anode supports with screen printed electrolyte layers (Figure 8). So whereas for screen printed electrolytes the reduced shrinkage in the anode support results in cracking of the electrolyte, for laminated layers it results in much denser anode supports, but with intact electrolyte layer. The observed differences in sintering behaviour probably stem from different processing routes and solids loadings in the screen printed layers and electrolyte tapes, respectively. The inks have been prepared by planetary milling and therefore show a slightly increased fraction of fine (d_{10} = 0.081 µm) particles as compared to the tape casting slips prepared by ordinary rotary milling (d_{10} = 0.12 µm). This fact and the higher solids

loading in the screen printed layers will cause an earlier onset of sintering for the electrolyte layer as compared to the anode support, creating stresses and eventually cracking of the electrolyte layer. The onset of sintering will be more closely matched for the laminated tapes, due to similarity of their solids contents and the reduced amount of fine YSZ particles. Other aspects to consider are the pressure involved in lamination and the use of various organics during processing. Lamination may cause increased packing and thus green density, thereby lowering the potential shrinkage of the electrolyte layer. The screen printed layers further contain a different binder system from the tapes, which may burn out at different temperatures than those used in the tape slips. This may lead to differential movements on firing, which could lead to cracking of a weak layer where binder has been burnt out but sintering has not yet started.

For optimum results tapes with identical solvent and plasticiser/binder systems should be used to aid the lamination process. Some pinholes can also be observed within the electrolyte layer, but it is expected that these can be eliminated through better de-airing of the slips prior to casting and lamination under clean room conditions.

The observed reaction layer at the anode – electrolyte interface will require further investigation to assure electronically conductive phases which could lead to short circuiting through the electrolyte are not formed. The reaction may be enhanced by the presence of a large amount of secondary TiO_2. It is currently believed that the cause for its occurrence lies predominantly within the processing conditions, rather than materials chemistry, since identical sintering conditions were used for screen printed and laminated half cells. Solvent mixing may be more prevalent during the lamination process as compared to screen printing, because an identical plasticiser/binder system is used in the former. Especially the plasticisers may mix extensively during the lamination process, which involves pressure and more elevated temperatures. Revision of used plasticisers may be necessary to avoid this mixing phenomenon.

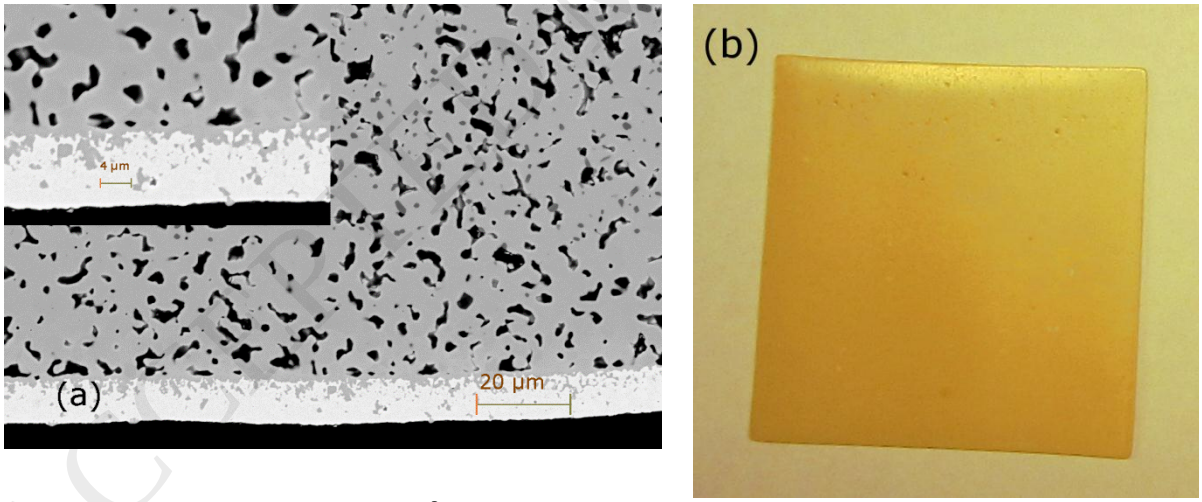

Figure 9: Scaled-up co-sintered 5 x 5 cm^2 half cell produced by laminating LSCT$_A$- (powder B) anode support and YSZ electrolyte tapes. Assembly co-sintered at 1325°C for 2 h. Figure (a) shows large presence of secondary phase within the electrolyte layer. Figure (b) shows a smooth electrolyte layer after firing.

Electrical properties

The electrical properties of porous and dense $La_{0.20}Sr_{0.25}Ca_{0.45}TiO_3$ ceramics, prepared both by die-pressing and small scale aqueous tape casting have been discussed previously [15,21]. The results from these studies suggest a variation in conductivity values, due to various sample densities, but also the effect of pre-reduction versus *in situ* reduction in 5% H_2 / 95% argon atmosphere. Additionally, changes in the material's stoichiometry and therefore defect

chemistry are expected to have major effects on the electrical properties. Electronic conduction is anticipated in A-site deficient strontium titanates under reducing conditions, due to the reduction of titanium:

$$2Ti_{Ti}^{\times} + O_O^{\times} \xrightarrow{H_2} 2Ti_{Ti}^{'} + V_O^{\cdot\cdot} + \tfrac{1}{2}O_2(g) \qquad (1)$$

The $Ti_{Ti}^{'}$ gives rise to metallic conduction at elevated temperatures. A degree of oxygen ion mobility may be expected as well, due to the formation of oxygen vacancies. Under oxidising conditions these titanates are semi-conducting, probably due to some mobile oxygen ions. For more information on strontium defect chemistry and its electrical properties under different conditions, the reader is referred to a recent review article [16]. To verify that the (scaled-up) processing methods in this study had not resulted in adverse effects on the electrical properties, both lab scale and scale-up anode supports were tested and compared to previous results.

Table 5: Samples tested for electrical properties in this study

Sample	Processing method	Powder	Porosity
A backbone	Lab scale	A	23
A + 10 wt.% CeO_2	Lab scale	A	23
A + 10 wt.% $Ce_{0.8}Gd_{0.2}O_{1.9}$	Lab scale	A	23
A + 10 wt.% $Ce_{0.5}Zr_{0.5}O_2$	Lab scale	A	23
B backbone	Scale-up (5 x 5 cm^2)	B	22
B + 10 wt.% CeO_2	Scale-up (5 x 5 cm^2)	B	22
B + 10 wt.% $Ce_{0.5}Zr_{0.5}O_2$	Scale-up (5 x 5 cm^2)	B	22

The samples tested are listed in Table 5. Their conductivity in air is shown in Figure 10a, clearly showing the strontium titanate material's semi-conductive behaviour. It shows a significant offset in the conductivity, with the powder B material being about 2.5 times more conductive at 850°C. Also striking is the difference in activation energies. The powder A derived anode support has an activation energy, E_a = 1.440 ± 0.003 eV, in excellent agreement with Yaqub et al. [21], whereas using powder B results in E_{act} = 1.150 ± 0.004. The lower activation energy is probably caused by the different chemical composition of this material, leading to increased oxygen ion mobility in the lattice. The results illustrate how the electrical properties are easily affected by changing the material's stoichiometry and thus defect chemistry.

The conductivity during *in situ* reduction of the two materials in anode supports is shown in Figure 10b. Reduction is carried out at 850°C in 5% H_2 / 95% argon atmosphere ($pO_2 = 10^{-20}$ – 10^{-21} bar). The results show very similar reduction kinetics and both materials exhibit similar conductivity values of around 3 S/cm after 16 hours of reduction. Small differences in the final conductivity values can easily be explained by small differences in pO_2 and microstructure. A previous study has suggested that the reduction kinetics and final conductivity values can be significantly improved by impregnation with ceria based catalysts [21]. The *in situ* reduction of anode supports impregnated with 10 wt.% of various ceria based catalysts is also shown in Figure 10b. Whereas large improvements in final conductivities are seen for the powder A derived ceramics, powder B based ceramics show little improvement upon impregnation. The mechanism by which impregnation affects the

electrical properties is currently poorly understood, but probably involves the formation of a solid solution between ceria and the titanate's surface layer to yield a more conductive phase than the original surface layer. Such a conductive phase would likely increase overall conductivity by lowering grain boundary resistivity. The fact that no such improvements are observed for powder B is most likely linked to the presence of secondary phases. It is possible that the impregnates preferably react with rutile TiO_2, to form phases which do not affect the overall electrical properties. In contrast to previous findings, the reduction kinetics seem hardly affected by impregnation. Modelling the conductivity data (after 4 hours reduction, when pO_2 is stable) to a generic exponential decay, according to equation (where $\sigma(0)$, $\sigma(t)$ and σ_∞ describe the conductivity values at time zero, time t and infinite time, respectively and τ the time constant), yields very similar time constants for all data sets, with τ in the range of 10 – 13 hours.

$$\frac{\sigma(t)-\sigma_\infty}{\sigma(0)-\sigma_\infty} = exp^{-\frac{t}{\tau}} \qquad (2)$$

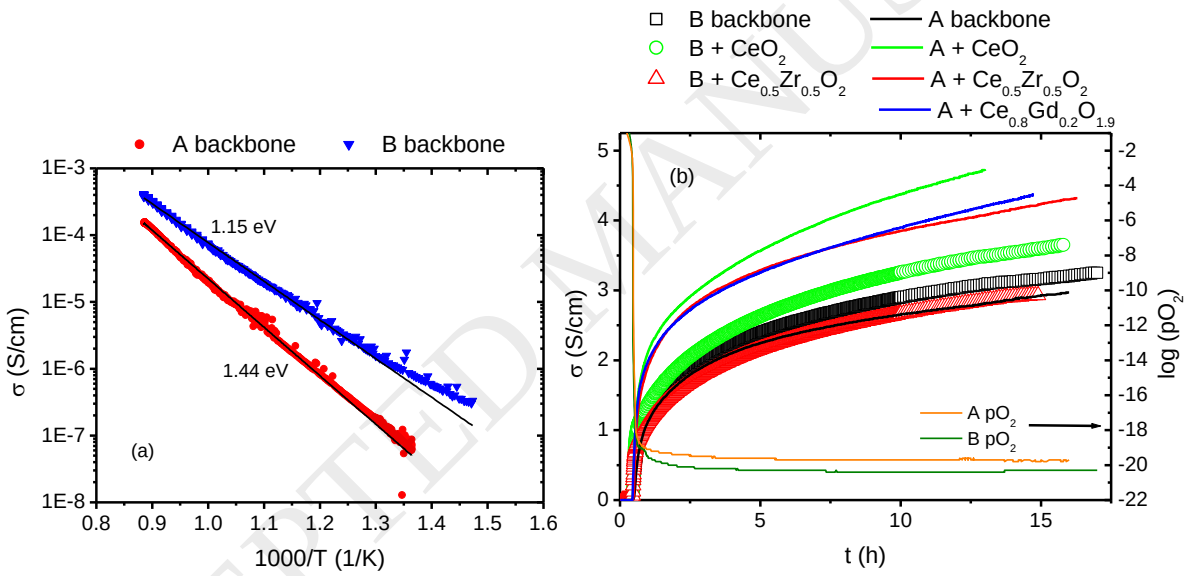

Figure 10: Left, conductivity as a function of temperature in air for $LSCT_A$- anode supports fabricated with powders A and B. Right, *in situ* reduction at 850°C in $pO_2 = 10^{-20} – 10^{-21}$ bar for anode supports with and without ceria based impregnates.

On comparison of the conductivity values obtained in this study with those obtained by Aljaberi on dense pre-reduced ($pO_2 \sim 10^{-20}$ bar, T = 1050°C) samples at 900°C, a reduction of roughly an order of magnitude is observed. This seems acceptable considering a porosity of about 20% and the *in situ* reduction at the lower temperature of 850°C. This also suggests that the processing methods applied in this study do not compromise the electrical properties of the anode support material, as to cause issues with current collection. Furthermore, changes in electrical properties due to microstructural differences between the lab scale and scaled up anode supports seem to play a minor role, as compared to the material's defect chemistry.

Mechanical properties

Initial tests concentrated on a determination of Young's modulus, characteristic strength, Weibull modulus and failure strain for dense and porous samples prepared by (small scale) tape casting. As an additional mechanical parameter, the resilience modulus (*U),* which is commonly used to assess metallic materials, was calculated from the determined mechanical parameters. The resilience modulus is a measure of the sample's ability to absorb energy during elastic deformation (energy-based method) and is defined by equation (3). $LSCT_{A-}$ ceramics for these first tests were fabricated using powder A and the respective results are summarised in Table 6.

$$U_r = \frac{\sigma^2}{2 \cdot E} \tag{3}$$

As expected, the porous samples show a lower characteristic strength and Young's modulus than their dense counterparts, where the Young's modulus appears to be more strongly affected. The Weibull modulus, as a measure of the spread in the strength data and hence in the width of the defect size distribution, is similar for the dense and porous materials. On the other hand, the fracture strain as a measure of the tolerance to applied strains is larger for the porous material, which might be an advantage with respect to tolerance of application-induced strains. Since the resilience modulus is basically a product of fracture strain and fracture strength, the improvement in fracture strain is also reflected to a minor extent in this parameter.

From SEM micrographs of the samples it was observed that large flaws are present in the samples prepared by small scale tape casting (Figure 11). These flaws are most likely due to entrapped air bubbles in the tapes. It is expected that the presence of these flaws limits the fracture stress and that a higher strength can be obtained by optimising the microstructure. The Young's modulus for porous samples could be related to the data of dense samples via the Phani-Niyogi (power-type) dependence (equation (4), where E_0 is the Young's modulus at zero porosity, P the porosity and a and n fitted constants [22]:

$$E = E_0 \cdot (1 - a \cdot P)^n \tag{4}$$

In previous studies for a similar perovskite (Y-doped strontium titanate) a and n were determined as 1.7 and 1.3, respectively [23]. The validity of equation (2) with these constants was performed based on three grades of the $LSCT_{A-}$ material (Table 3). The Young's modulus of completely dense material was calculated for every measurement point based on the measured effective Young's modulus. The average value E_0 was determined as 209 GPa with 8 GPa standard deviation (coefficient of variation = 0.04). The fitting is considered to be satisfying, and hence the effective Young's modulus of further $LSCT_{A-}$ material charges can be estimated with $E = 209 \cdot (1\text{-}1.7 \cdot P)^{1.3}$ requiring only a porosity value.

It was expected that large scale processing under optimised conditions at DTU would result in more homogeneous microstructures and reduce the number and size of flaws. Powder B was used during all of the scale-up work. The mechanical results of $LSCT_{A-}$ – YSZ half-cells prepared by large scale processing are also shown in Table 6. These results reveal that all mechanical parameters are inferior compared to samples prepared by small scale, non-optimised, tape casting. Only the Weibull modulus gives a slight indication of a more homogeneous defect distribution, nevertheless the value is still far from the values of typical

engineering ceramics (*e.g.* 8 – 20 for Al_2O_3; 10 – 15 for ZrO_2; ~40 for cast iron and ~100 for steel [24]). Microscopic investigations presented in Figure 11 however, do indicate a superior microstructural quality as compared to small scale fabrication. So despite similar porosities, but apparent superior microstructure and absence of large flaws, the use of powder B has led to a significant reduction of the mechanical parameters.

Similar as verified for standard Ni/YSZ SOFC cells, it is not believed that the presence of the 10 µm thin electrolyte layer affects the mechanical properties [25]. Some strain may have resulted from the co-sintering, but this should not have reduced the mechanical strength significantly. Slightly different thermal histories due to different furnaces for small scale and scale-up is also a factor which could lead to different mechanical properties. However, the most likely cause for the reduced mechanical properties of scaled up cells would be a reduction in the inter-grain bond strength due to the presence of appreciable amounts of secondary phase rutile TiO_2 within grain boundaries . The change in composition of the main $LSCT_{A-}$ phase as suggested by phase analysis and electrical characterisation might cause some changes in sintering characteristics, but is not expected to play a dominant role [16,26,27].

Table 6: Comparison of the mechanical parameters obtained for $LSCT_{A-}$ specimens (room temperature values).

Parameter	$LSCT_{A-}$ Dense (powder A) (small scale)	$LSCT_{A-}$ Porous (powder A) (small scale)	$LSCT_{A-}$-YSZ Half-cell **(**powder B**)** (scaled up)
Porosity (%)	3	23	21
Young's modulus* [GPa]	202 ± 17	105 ± 2	119 ± 23
Characteristic strength [MPa]	80 ± 7	66 ± 6	44 ± 3
Weibull modulus	3.6 ± 1.1	3.3 ± 1.0	4.7 ± 1.4
Failure strain [%]	0.040 ± 0.005	0.063 ± 0.015	0.037 ± 0.008
Resilience modulus [kJ/m^3]	15.8 ± 2.7	20.7 ± 5.9	8.3 ± 1.9

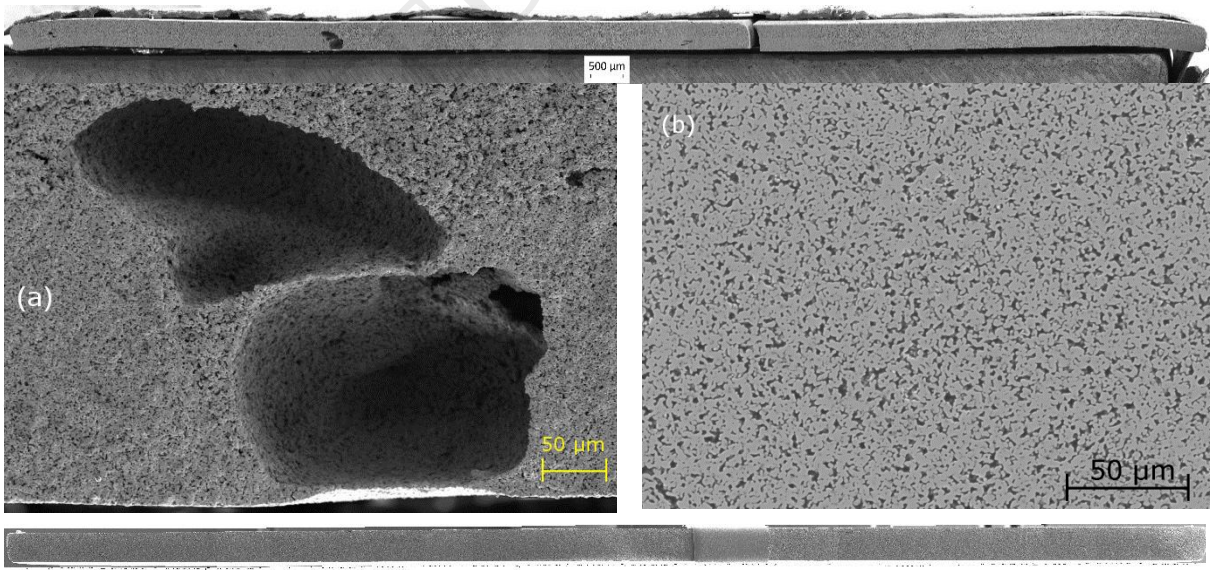

Figure 11: Micrographs of different batches of $LSCT_{A-}$ samples for mechanical testing. Top and zoomed section (a): ceramic produced by non-optimised small scale tape casting using powder A, showing large (~100 - 200 µm) defects due to air entrapment. Bottom: ceramic produced by optimised large scale tape casting at DTU using powder B, showing absence of major flaws and generally superior microstructure as seen in zoomed section (b) .

The characteristic strengths and Young's Moduli measured for the $LSCT_{A-}$ anode supports and half cells compare well, in both cases, with previous findings on a similar material, $Y_{0.07}Sr_{0.895}TiO_3$ [23,28]. However, they are lower than values reported in literature for Ni/YSZ cermets, even though there seems to be a large spread in the latter, i.e. 100 – 300 MPa [28–32]
. It is however expected that the strength of $LSCT_{A-}$ ceramics without TiO_2 contamination can be improved significantly by avoiding the large flaws as shown in Figure 11. When comparing the resilience moduli, the value for $LSCT_{A-}$ is lower by an order of magnitude as compared to Ni/YSZ [32,34]. This can be explained by the presence of metallic nickel in the cermet, which due its elastic properties reduces the Young's modulus and thus increases the resilience modulus. However, the effects of long term SOFC operation, such as creep and Ni sintering, on the mechanical strength in Ni/YSZ anode supports are still under-investigated. Such changes would certainly not play a role in fully ceramic strontium titanate anode supports. More in depth mechanical testing will be required (elevated temperatures, reducing/oxidising conditions, etc.) to determine whether an all ceramic anode support will be strong enough for SOFC stacking and operation.

Conclusions

The transfer of ceramic formulations and methods developed in the lab to an industrial environment still forms a serious barrier to the successful implementation of many novel materials into commercial SOFC and other applications. In this study it has been proven possible to fabricate anode supported half cells on a technically relevant scale, using such a novel ceramic anode material. Moreover, the paper discusses processing techniques, which are industrially relevant and suitable for further scaling up, which to our knowledge is a first attempt at such a feature. Lamination of aqueous anode support and electrolyte tapes was shown to yield superior sintered half cells as compared to depositing electrolyte layers by screen printing. Current challenges are to fine tune anode support porosities and electrolyte densities, through careful matching of shrinkages of the two components. Future fuel cell tests on such cells may verify whether the current levels of porosity are sufficiently high for effective gas transport and catalyst impregnation. However, the use of pore formers may be required if electrochemical testing shows the porosity to be too low. Such tests would also indicate whether the electronic conductivity of A-site deficient La doped strontium titanates is sufficient for relevant operating conditions. Previous work has shown this new anode material is suitable in an electrolyte supported cell design, but the lower operating temperature for anode supported cells may create an additional challenge in reducing the titanates to a sufficient level.
This study also confirms the importance of stoichiometry on the materials and defect chemistry of doped strontium titanates. The use of two powders with supposedly identical, but effectively different stoichiometries has led to significant changes in both electrical and mechanical properties. Carefully controlling the stoichiometries of these novel materials is therefore paramount in guaranteeing good anode performance and mechanical support. Controlling these stoichiometries from batch to batch may be a future challenge for powder producers as larger quantities are required for scale up. In this respect, it would have made more sense to use powder A for our scale-up efforts, due to its superior structural and electrical properties, but as mentioned this was unfortunately no option during this study.

Acknowledgements

The authors gratefully acknowledge funding from the Fuel Cells and Hydrogen Joint Undertaking under grant agreement n° 256730. Angus Calder and Sylvia Williamson are also acknowledged for carrying out XRF and BET measurements, respectively.

References

[1] L. Blum, P. Batfalsky, Q. Fang, L.G.J. de Haart, J. Malzbender, N. Margaritis, N.H. Menzler, R. Peters, SOFC Stack and System Development at Forschungszentrum Jülich, J. Electrochem. Soc. 162 (2015) F1199–F1205.

[2] J. Malzbender, R.W. Steinbrech, L. Singheiser, A review of advanced techniques for characterising SOFC behaviour, Fuel Cells. 9 (2009) 785–793.

[3] M.C. Verbraeken, B. Iwanschitz, A. Mai, J.T.S. Irvine, Evaluation of Ca Doped La0.2Sr0.7TiO3 as an Alternative Material for Use in SOFC Anodes, J. Electrochem. Soc. 159 (2012) F757–F762.

[4] M.C. Verbraeken, B. Iwanschitz, E. Stefan, M. Cassidy, U. Weissen, A. Mai, J.T.S. Irvine, Short Stack and Full System Test Using a Ceramic A-Site Deficient Strontium Titanate Anode, Fuel Cells. (2015) 682–688.

[5] V. Vasechko, M. Ziegner, J. Malzbender, Influence of phase transformations on mechanical properties of novel ceramics for solid oxide fuel cell anode applications, Ceram. Int. 40 (2014) 13179–13189.

[6] L.Y. Lu, M.C. Verbraeken, M. Cassidy, J.T.S. Irvine, A Solid Oxide Fuel Cell with Lanthanum and Calcium Co-Doped Strontium Titanate as Support, Solid Oxide Fuel Cells 13 SOFC-XIII. 57 (2013) 1415–1422.

[7] M.C. Verbraeken, M. Cassidy, J.T.S. Irvine, Aqueous Processing Routes for New SOFC Materials, in: Adv. Solid Oxide Fuel Cells IX, John Wiley & Sons, Inc., 2013: pp. 67–76. http://dx.doi.org/10.1002/9781118807750.ch6.

[8] S. Lee, G. Kim, J.M. Vohs, R.J. Gorte, SOFC anodes based on infiltration of La(0.3)Sr(0.7)TiO(3), J. Electrochem. Soc. 155 (2008) B1179–B1183.

[9] G. Kim, M.D. Gross, W. Wang, J.M. Vohs, R.J. Gorte, SOFC anodes based on LST-YSZ composites and on Y0.04Ce0.48Zr0.48O2, J. Electrochem. Soc. 155 (2008) B360–B366.

[10] A. Hagen, M. Menon, R. Barfod, P.V. Hendriksen, S. Ramousse, P.H. Larsen, Properties and performance of SOFCs produced on a pre-pilot plant scale, Fuel Cells. 6 (2006) 146–150.

[11] Q.L. Ma, F. Tietz, A. Leonide, E. Ivers-Tiffee, Anode-supported planar SOFC with high performance and redox stability, Electrochem. Commun. 12 (2010) 1326–1328.

[12] Q.L. Ma, F. Tietz, A. Leonide, E. Ivers-Tiffee, Electrochemical performances of solid oxide fuel cells based on Y-substituted SrTiO(3) ceramic anode materials, J. Power Sources. 196 (2011) 7308–7312.

[13] P. Gordes, N. Christiansen, E.J. Jensen, J. Villadsen, Synthesis of Perovskite-Type Compounds by Drip Pyrolysis, J. Mater. Sci. 30 (1995) 1053–1058.

[14] L.J. Van der Pauw, A method of measuring specific resistivity and Hall effect of discs of arbitrary shape, Philips Res. Rep. 13 (1958) 1–9.

[15] A.D. Aljaberi, J.T.S. Irvine, Ca-substituted, A-site deficient perovskite La0.2Sr0.7TiO3 as a potential anode material for SOFCs, J. Mater. Chem. A. 1 (2013) 5868–5874.

[16] M.C. Verbraeken, T. Ramos, K. Agersted, Q. Ma, C.D. Savaniu, B.R. Sudireddy, J.T.S. Irvine, P. Holtappels, F. Tietz, Modified strontium titanates: from defect chemistry to SOFC anodes, RSC Adv. 5 (2015) 1168–1180.

[17] H.F. Mark, Encyclopedia of polymer science and technology, Wiley, 2007.

[18] R.E. Mistler, E.R. Twiname, Tape casting: Theory and Practice, Wiley, 2006.
[19] M. Pihlatie, A. Kaiser, P.H. Larsen, M. Mogensen, Dimensional Behaviour of Ni-YSZ Anode Supports for SOFC Under RedOx Cycling Conditions, Solid Oxide Fuel Cells 10 Sofc-X Pts 1 2. 7 (2007) 1501–1510.
[20] M. Cassidy, D.J. Doherty, X. Yue, J.T.S. Irvine, Development of Tailored Porous Microstructures for Infiltrated Catalyst Electrodes by Aqueous Tape Casting Methods, ECS Trans. 68 (2015) 2047–2056.
[21] A. Yaqub, C. Savaniu, N.K. Janjua, J.T.S. Irvine, Preparation via a solution method of La0.2Sr0.25Ca0.45TiO3 and its characterization for anode supported solid oxide fuel cells, J. Mater. Chem. A. 1 (2013) 14189–14197.
[22] K.K. Phani, S.K. Niyogi, YOUNG MODULUS OF POROUS BRITTLE SOLIDS, J. Mater. Sci. 22 (1987) 257–263.
[23] V. Vasechko, B. Huang, Q. Ma, F. Tietz, J. Malzbender, Thermomechanical properties of Y-substituted SrTiO3 used as re-oxidation stable anode substrate material, J. Eur. Ceram. Soc. 34 (2014) 3749–3754.
[24] J. Roesler, H. Harders, M. Baeker, Mechanical Behaviour of Engineering Materials, Springer, 2006.
[25] J. Malzbender, R.W. Steinbrech, L. Singheiser, FAILURE PROBABILITY OF SOLID OXIDE FUEL CELLS, in: 29th Int. Conf. Adv. Ceram. Compos., Cocoa Beach, FL, 2005: pp. 293–298. <Go to ISI>://WOS:000273628400033.
[26] A. Ianculescu, A. Braileanu, M. Zaharescu, S. Guillemet, I. Pasuk, J. Madarasz, G. Pokol, Formation and properties of some Nb-doped SrTiO3-based solid solutions, J. Therm. Anal. Calorim. 72 (2003) 173–180.
[27] D. Neagu, J.T.S. Irvine, Structure and Properties of La0.4Sr0.4TiO3 Ceramics for Use as Anode Materials in Solid Oxide Fuel Cells, Chem. Mater. 22 (2010) 5042–5053.
[28] B.X. Huang, V. Vasechko, Q.L. Ma, J. Malzbender, Thermo-mechanical properties of (Sr,Y)TiO3 as anode material for solid oxide fuel cells, J. Power Sources. 206 (2012) 204–209.
[29] N.H. Menzler, J. Malzbender, P. Schoderböck, R. Kauert, H.P. Buchkremer, Sequential Tape Casting of Anode-Supported Solid Oxide Fuel Cells, Fuel Cells. 14 (2014) 96–106.
[30] N. Christiansen, J.B. Hansen, H. Holm-Larsen, S. Linderoth, P.H. Larsen, P.V. Hendriksen, A. Hagen, Solid Oxide Fuel Cell Development at Topsoe Fuel Cell A/S and Riso National Laboratory, Solid Oxide Fuel Cells 10 Sofc-X Pts 1 2. 7 (2007) 31–38.
[31] W. Schafbauer, N.H. Menzler, H.P. Buchkremer, Tape Casting of Anode Supports for Solid Oxide Fuel Cells at Forschungszentrum Julich, Int. J. Appl. Ceram. Technol. 11 (2014) 125–135.
[32] A. Nakajo, J. Kuebler, A. Faes, U.F. Vogt, H.J. Schindler, L.-K. Chiang, S. Modena, J. Van herle, T. Hocker, Compilation of mechanical properties for the structural analysis of solid oxide fuel cell stacks. Constitutive materials of anode-supported cells, Ceram. Int. 38 (2012) 3907–3927.
[33] J. Malzbender, R.W. Steinbrech, Threshold fracture stress of thin ceramic components, J. Eur. Ceram. Soc. 28 (2008) 247–252.
[34] S. Biswas, T. Nithyanantham, S. Nambiappan Thangavel, S. Bandopadhyay, High-temperature mechanical properties of reduced NiO–8YSZ anode-supported bi-layer SOFC structures in ambient air and reducing environments, Ceram. Int. 39 (2013) 3103–3111.